

## A CASPT2 Description of the Electronic Structures of $\text{FeO}_3^{-/0}$ in Relevance to the Anion Photoelectron Spectrum

Van Tan Tran and Marc F. A. Hendrickx\*

*Afdeling Kwantumchemie en Fysicochemie, Departement Chemie, Katholieke Universiteit Leuven, Celestijnenlaan 200F, B-3001 Heverlee-Leuven, Belgium*

Received September 15, 2010

**Abstract:** DFT and multireference methods were used to investigate the electronic structure of  $\text{FeO}_3$  and  $\text{FeO}_3^-$  clusters. Geometries of different spin multiplicities and conformations were optimized without any symmetry restrictions at the BP/QZVP level and further refined with the CASPT2 method. Although the latter type of calculations were performed by using the  $C_{2v}$  point group, all low-lying states relevant to the photoelectron spectrum were found to correspond to or to resemble closely a planar  $D_{3h}$  iron trioxide with no bonds between the oxygen atoms. Depending on the computational method used, the ground state of the  $\text{FeO}_3^-$  anion can be either  $^2E''$  or  $^4A_1'$ . The two lowest binding energy bands of the photoelectron spectrum of  $\text{FeO}_3^-$  can only be ascribed to electron detachments from the  $^2E''$  state. The first band is the result of a transition to the  $^1A_1'$  ground state of  $\text{FeO}_3$ , whereas the second band originates from the first excited  $^3E''$  state. A harmonic vibrational analysis of the symmetric stretch shows that the observed vibrational progressions of these two bands in the photoelectron spectrum of  $\text{FeO}_3^-$  are also in line with the assignment. A molecular orbital analysis led to the conclusion that the electronic structures of the anionic and neutral clusters can formally be described by an oxidation state of iron of +5 and +6, respectively. A population analysis, on the contrary, points to an ionization that takes place on the oxygen atoms.

### Introduction

Iron oxide clusters  $\text{FeO}_n$  can serve as basic models for numerous biological systems<sup>1,2</sup> that play important roles, such as oxygen transportation. In an industrial context, they are also of importance because they bear relevance to the main factor in redox processes like iron corrosion<sup>3</sup> and as a model for various catalysts.<sup>4–8</sup> To understand the electronic structures of  $\text{FeO}_n/\text{FeO}_n^-$ , Wang and co-workers synthesized  $\text{FeO}_n^-$  ( $n = 1–4$ ) in the gas phase and investigated their photoelectron spectroscopy (PES) experimentally by using lasers with photon energies of 3.49 and 4.66 eV.<sup>9–12</sup> More than a decade ago, Chertihin and co-workers also observed the neutral systems of these clusters by infrared spectroscopy as products of the reaction of laser-ablated Fe atoms with oxygen molecules in a condensing argon stream.<sup>13</sup> By

analyzing their infrared spectra in detail and with the aid of calculations, the authors proposed and confirmed the existence for various stable conformations of iron–oxygen clusters. Their theoretical work comprised geometry optimizations and harmonic frequency calculations at the BP/DZVP level. Also, results obtained by the B3LYP hybrid technique with a (15s12p6d1f)/[9s7p4d1f] basis set for iron and 6-311+G(2df) basis set for oxygen were given. A few years later, density functional theory (DFT) calculations employing the 6-311+G\* basis sets and the BPW91 functional were performed by Gutsev et al.,<sup>14</sup> mainly with the purpose of calculating the electron affinities of  $\text{FeO}_n$ . Rather recently, a combined experimental and theoretical study on the neutral  $\text{FeO}_3$  was carried out by Yu et al.<sup>15</sup> by using matrix infrared spectroscopy combined with DFT calculations. To date, all experimental and computational works agree on a stable  $\eta^2\text{-O}_2\text{FeO}$  complex that is characterized by a quintet lowest state of planar  $C_{2v}$  symmetry and a more

\* Corresponding author. E-mail: marc.hendrickx@chem.kuleuven.be.

stable iron trioxide possessing a planar singlet ground state of  $D_{3h}$  symmetry. A detailed description of the electronic structure of the monoiron oxide molecules is however still needed.

Unsaturated complexes of the type at hand are known to possess many low-lying states of different spin multiplicities.<sup>14,16–24</sup> As a consequence, for the identification of their ground states and all possible low-lying excited states, a multireference wave function method turns out to be a very convenient tool. Indeed, these methods, such as CASPT2 (complete active space second-order perturbation theory) or MRCI (multireference configuration interaction), were applied successfully for the description of the electronic structures of  $\text{FeO}/\text{FeO}^-$ <sup>25,26</sup> and  $\text{FeO}_2/\text{FeO}_2^-$ .<sup>27</sup> It is very surprising that the electronic structures of the higher monoiron oxides clusters, such as  $\text{FeO}_3^{-/0}$ , are still not studied at any of these computational levels and, therefore, remain a bit of a mystery. More specifically, the additional electron was found to be delocalized over the three oxygen atoms,<sup>13</sup> whereas in recent CASPT2 studies it was argued that these clusters can be described as transition metal complexes, implying that the valence orbitals have predominantly 3d metal character.<sup>17,19,25</sup> In this contribution, we present a multireference wave function study on the basis of the CASPT2 method for  $\text{FeO}_3$  and  $\text{FeO}_3^-$ , containing a detailed picture for their electronic structures. The accuracy of the presented results are tested against the experimental photoelectron spectrum of  $\text{FeO}_3^-$ .

## Computational Details

In the first step of our study, the geometries of different spin multiplicities from singlet to sextet of  $\text{FeO}_3$  and  $\text{FeO}_3^-$  are optimized by an unrestricted DFT technique with the QZVP basis sets<sup>28</sup> and the BP86 functional<sup>29</sup> as implemented in the TURBOMOLE 5.10 suite of programs.<sup>30</sup> The geometry optimizations were done without symmetry restrictions so that all structural parameters are allowed to relax and the lowest energy electronic states of either of the two molecules are serious candidates for their actual ground states. At all of these optimized geometries, a harmonic vibrational frequency calculation is carried out to ensure that the structures found are true minima and not saddle points.

In the second step, we utilized the efficient MOLCAS 7.4 package<sup>31</sup> to perform CASPT2 calculations. Since only Abelain point groups are implemented in this computational package, all of the calculations were carried out using  $C_{2v}$  symmetry, although some optimized DFT geometries exhibit a higher  $D_{3h}$  symmetry. As illustrated in Figure 1, the molecule is placed in the  $yz$  plane with one oxygen atom along the  $z$  axis. The basis sets used are [8s,7p,5d,4f,2g] and [6s,5p,4d,2f] ANO-RCC, for iron and oxygen, respectively.<sup>32</sup> Scalar relativistic effects are included by the Douglas–Kroll formalism.<sup>33,34</sup> The orbitals for the CASPT2 calculations are obtained from complete active space self-consistent field (CASSCF) calculations, for which the active spaces include the 2p orbitals of oxygen and the 3d and 4s orbitals of iron. Corresponding to either the neutral or anionic system, we have a total of 20 or 21 electrons in 15 orbitals. The

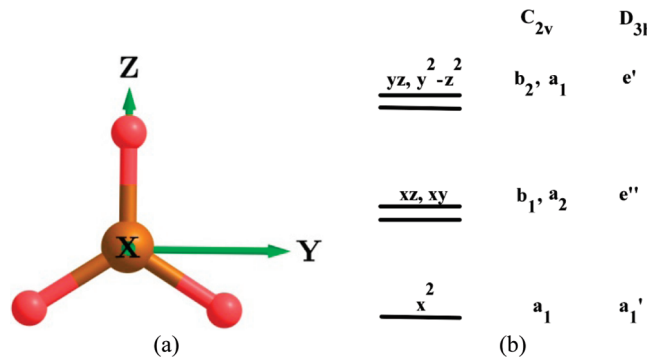


**Figure 1.** (a) Choice of the coordination system for the CASPT2 calculations. (b) Qualitative orbital energy scheme for the valence d orbitals.

CASPT2 calculations correlated the 3p, 3d, and 4s orbitals of iron and 2s and 2p orbitals of oxygen, whereas at this level the intruder states problem was addressed by applying an imaginary shift. The BP/QZVP structures were refined using numerical gradient CASPT2 optimization. From these structures, adiabatic detachment energies (ADEs) and vertical detachment energies (VDEs) for  $\text{FeO}_3^-$  were evaluated. In order to improve our results, single point calculations with the larger ANO-RCC basis set [8s,7p,6d,4f,2g,1h] for iron and [7s,6p,4d,3f,1g] for oxygen were performed.

## Results and Discussion

Both previous DFT studies<sup>14,15</sup> showed that the  $\text{FeO}_3$  systems can have two relatively low-lying conformations. One that does not possess any O–O bonds is denoted as  $O_3\text{Fe}$ , whereas another has one O–O bond and corresponds to  $\eta^2\text{-O}_2\text{FeO}$ . Linear structures of the type O–Fe–O–O were calculated at energies 50 kcal/mol higher than the ground state.<sup>13</sup> With the purpose of investigating the photoelectron spectrum of  $\text{FeO}_3^-$ , we therefore do not need to consider them in our study. In order to be sure about the low-lying states of both anion and neutral systems, we reoptimized various spin multiplicities of  $O_3\text{Fe}$  and  $\eta^2\text{-O}_2\text{FeO}$  at the BP/QZVP level. The results are summarized in Figure 2, which contains the structural parameters for the various conformations and their relative energies. For the  $O_3\text{Fe}$  conformation, the ground state of the neutral system clearly turns out to be a singlet state with  $D_{3h}$  symmetry, while the ground state of the anion can be either a doublet possessing  $C_{2v}$  symmetry or a quartet with  $D_{3h}$  symmetry. Indeed, the quartet is predicted at this computational level to be just 0.02 eV higher in energy than the doublet. Our DFT calculations predict a value  $1023 \text{ cm}^{-1}$  for the antisymmetric stretching modes of the singlet ground state, see Table 1, which is in fairly good agreement with the experimental values of  $975.8 \text{ cm}^{-1}$  and  $950 \text{ cm}^{-1}$  obtained from the infrared spectrum in a argon matrix.<sup>13,15</sup> For the  $\eta^2\text{-O}_2\text{FeO}$  conformation and in accordance with previous theoretical work, we could identify a quintet of  $C_s$  symmetry and a quartet of  $C_{2v}$  symmetry as the lowest states of the neutral and anionic systems, respectively. Our predicted vibrational frequencies of  $933 \text{ cm}^{-1}$  and  $1052 \text{ cm}^{-1}$  for this quintet are in good agreement with the infrared bands at  $1148 \text{ cm}^{-1}$  and  $928 \text{ cm}^{-1}$  of ref

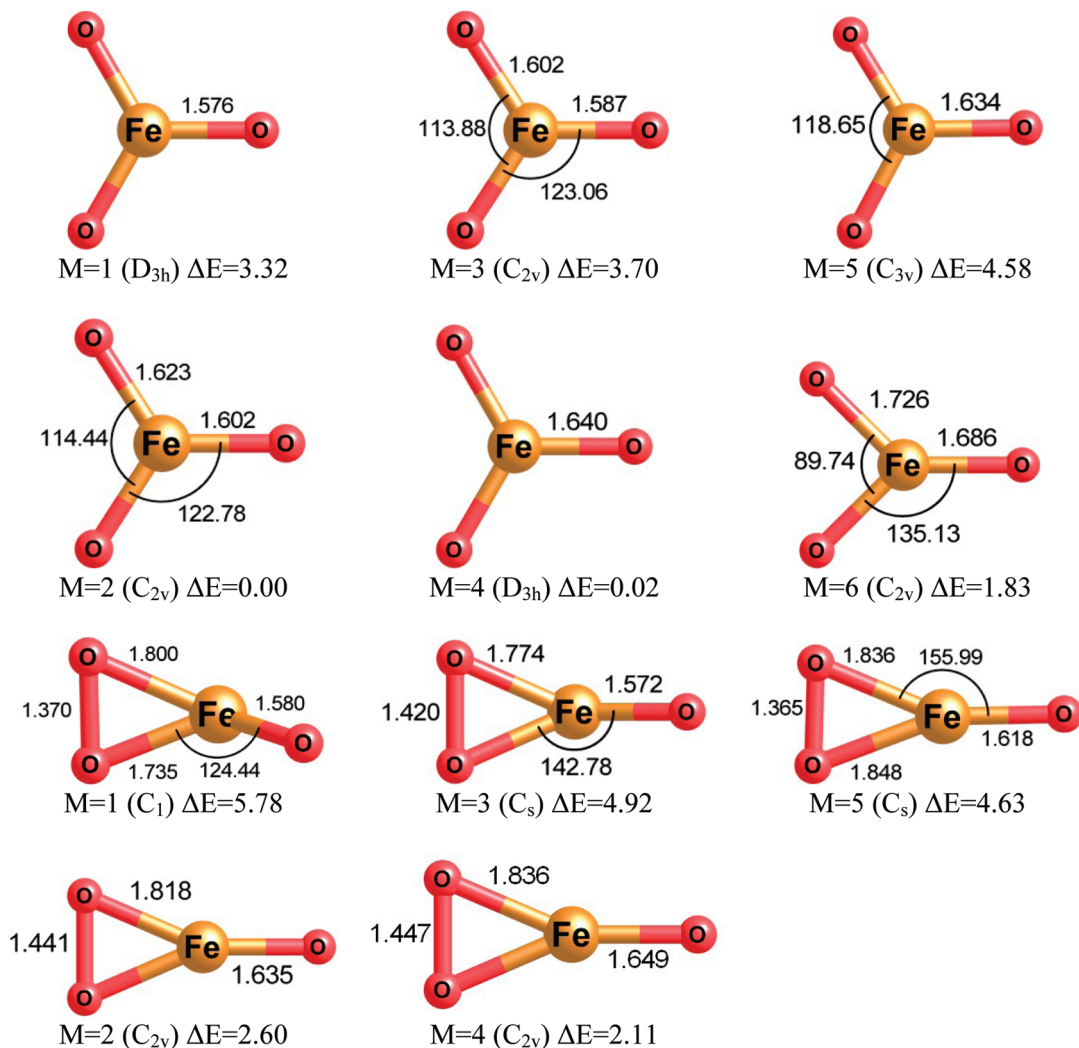


**Figure 2.** Structures (bond distances in Ångstroms and bond angles in degrees) and relative energies (eV) of  $\text{FeO}_3$  and  $\text{FeO}_3^-$  as obtained by BP/QZVP calculations.

13 and the corresponding  $1002 \text{ cm}^{-1}$  band of ref 15 as well as with the DFT values mentioned in both papers. The predicted quintet lowest energy state of  $\eta^2\text{-O}_2\text{FeO}$  is, energetically, 1.3 eV higher than the singlet ground state of the  $\text{O}_3\text{Fe}$  conformation. For the anionic conformations, the quartet of  $\eta^2\text{-O}_2\text{FeO}^-$  is 2.11 eV higher than the doublet state of  $\text{O}_3\text{Fe}$ , which was calculated as the ground state of the  $\text{FeO}_3^-$  anion. Because of this large energy difference, it is safe to base our assignment of the photoelectron spectroscopy of  $\text{FeO}_3^-$  only on the  $\text{O}_3\text{Fe}$  conformation. With this information at hand, we only investigated the  $\text{O}_3\text{Fe}^{-/0}$  conformations in our subsequent CASPT2 calculations, which we will simply denote as  $\text{FeO}_3^{-/0}$ .

Starting from the optimized geometries of the previous DFT calculations, we first performed for each specific spin multiplicity CASPT2 single point calculations for the purpose of finding the lowest energy state for each irreducible representation of the  $\text{C}_{2v}$  point group. In a next step, all possible low lying states were reoptimized at the CASPT2 level by employing the small ANO-RCC basis set as mentioned in the Computational Details. In Figure 3, we present the optimized structures of the  ${}^1\text{A}_1$ ,  ${}^3\text{A}_2$ ,  ${}^3\text{B}_1$ ,  ${}^2\text{A}_2$ ,  ${}^2\text{B}_1$ , and  ${}^4\text{B}_2$  states. The structural parameters of these states

were found to be nearly unchanged from the DFT geometries of the same multiplicity. To a certain extent, this confirms that we have found the lowest energy states. For the neutral  $\text{FeO}_3$ , there can be little doubt about its ground state. This is clearly the  ${}^1\text{A}_1$ , while at 0.34 eV higher in energy we calculated the first excited state as  ${}^3\text{A}_2$ . This result is more or less coherent with the DFT calculations. For  $\text{FeO}_3^-$ , there is a contradiction between CASPT2 and DFT concerning the prediction of the ground state. The  ${}^4\text{B}_2$  state is now 0.27 eV lower than the  ${}^2\text{A}_2$  state. However, this energy difference is only just outside the believed error margin of the CASPT2 method. Furthermore, by taking into account that at the employed computational level it is likely to overestimate the relative stability of the higher spin state, we cannot make an absolute statement about the true ground state of  $\text{FeO}_3^-$ . We believe that a more secure statement about the ground state of  $\text{FeO}_3^-$  most likely needs a more accurate treatment of the electronic dynamic correlation energy.

The CASPT2 geometry optimization shows that the symmetry of  ${}^4\text{B}_2$  and  ${}^1\text{A}_1$  is actually  $D_{3h}$  while the symmetry of  ${}^2\text{A}_2$  and  ${}^3\text{A}_2$  is  $\text{C}_{2v}$ . These  $\text{C}_{2v}$  structures exhibit only a slight distortion from  $D_{3h}$  symmetry as a result of weak Jahn–Teller effects. From single point CASPT2 calculations,

**Table 1.** Relative Energies (RE), Harmonic Unscaled Vibrational Frequencies ( $\text{cm}^{-1}$ ), and Intensities (km/mol) for the Two Studied Conformations of  $\text{FeO}_3$  and  $\text{FeO}_3^-$  at the BP/QZVP Level

cluster	spin multiplicity	RE (eV)	frequency (intensity)
$\text{O}_3\text{Fe}^-$	2	0.00	195 (50), 237 (3), 335 (0), 817 (407), 856 (0), 969 (197)
	4	0.02	178 (52), 310 (0), 311 (0), 819 (0), 913 (204), 914 (204)
	6	1.83	120 (7), 143 (47), 217 (0), 689 (4), 732 (6), 811 (148)
$\text{O}_3\text{Fe}$	1	3.33	147 (11), 332 (0), 333 (0), 920 (0), 1023 (101), 1023 (101)
	3	3.70	99 (41), 200 (22), 345 (0), 864 (1), 865 (175), 995 (92)
	5	4.58	80 (33), 219 (0) 223 (0), 605 (2), 606 (2), 837 (2)
	2	2.60	86 (1), 126 (1), 438 (7), 561 (6), 882 (13), 936 (288)
	4	2.11	130 (11), 165 (9), 537 (6), 549 (10), 869 (30), 918 (317)
$\eta^2\text{-O}_2\text{FeO}^-$	1	5.78	158 (7), 234 (18), 526 (3), 637 (1), 967 (101), 1023 (166)
	3	4.92	122 (19), 187 (16), 394 (16), 571 (4), 938 (15), 1002 (200)
	5	4.63	44 (15), 146 (24), 506 (1), 611 (2), 933 (16), 1052 (174)

as given in Tables 2 and 4, we know that  ${}^4\text{B}_2$  and  ${}^1\text{A}_1$  are nondegenerate states, while  ${}^2\text{A}_2$  and  ${}^2\text{B}_1$  and  ${}^3\text{A}_2$  and  ${}^3\text{B}_1$  are degenerate  $\text{D}_{3\text{h}}$  states. In both cases, they are the two components of  $\text{E}''$  states. A graphical representation for the potential energy curves of the low-lying states is given in Figure 4. Here, a geometry optimization for the low lying states within  $\text{D}_{3\text{h}}$  symmetry is performed by carrying out CASPT2 single point calculations for a number of Fe–O bond distances, around the respective equilibrium bond distances. Although the calculations were carried out within the broken symmetry approach, the  $\text{A}_2$  and  $\text{B}_1$  curves are shown to be nearly degenerated; the scale used on the ordinate axis places the states at the same points on the two graphs of the  ${}^2\text{E}''$  and  ${}^3\text{E}''$  states. The energetic Jahn–Teller effects on both states were further examined by performing a CASPT2 geometry optimization for their  $\text{B}_1$  components, a procedure that takes full account of these effects as applied previously on the related  $\text{FeO}_4^{-/0}$  clusters at the DFT level.<sup>35,36</sup> The results are given Table 2 and are depicted in Figure 3 and show only small changes in geometry. Indeed, the bond distances between two  $\text{E}''$  components vary about 1/100 of an Ångstrom. Bond angles between the  $\text{A}_2$  and  $\text{B}_1$  components differ only by a few degrees. There is here however a systematic trend that can be observed. The  $\text{B}_1$  component has two bond angles smaller than the  $\text{D}_{3\text{h}}$  value of  $120^\circ$  and consequently a third bond angle that has increased from this high symmetry value. The opposite is found for the  $\text{A}_2$  components. As a result of having two larger bond angles, the remaining angle decreases noticeably further from  $120^\circ$  in these components. The equilibrium distances of the bonds that are involved in the smaller bond angles are partly larger due to the increased electrostatic repulsion between the negatively charged oxygens. A further explanation for these geometric differences will be discussed after a detailed molecular orbital analysis of the electronic structure

of the states in the following paragraph. As Jahn–Teller effects decrease the energy, the  $\text{A}_2$  states are stabilized more since they possess the largest distortions. This causes  ${}^2\text{A}_2$  and  ${}^3\text{A}_2$  to become the lowest excited CASPT2 states of  $\text{FeO}_3^-$  and  $\text{FeO}_3$ , respectively. Energetically, the effects are indeed very small. The difference between the two components is calculated to be on the order of a few hundredths of an electronvolt in Table 2. These values are by far too small to induce any effect on the experimental photoelectron spectra or to have a measurable effect on the electron affinity.

As mentioned in the previous paragraph, there is a need for an in-depth description of the electronic structure of  $\text{FeO}_3^-$ . In view of the intended assignment of the photo-electron spectrum, this is best done in relationship with its neutral counterpart. For doing so, we made plots of the molecular orbitals of the active spaces for all relevant states. These plots for the  ${}^4\text{B}_2$  CASPT2 ground state, classified according to the irreducible representation of the  $\text{C}_{2\text{v}}$  point group and accompanied by their CASSCF natural occupation numbers, are depicted in Figure 5. A comparison with similar orbitals obtained with the CASSCF calculations on all mentioned states shows that the valence orbitals of the studied molecules, i.e., the orbitals with occupation numbers in the vicinity of one, have always a predominant iron 3d character. Further observation shows that they are of an antibonding nature between iron and the adjacent oxygen atoms. From the entry for the leading configuration of  ${}^4\text{B}_2$  in Table 4, we learn that the three unpaired electrons of this quartet state are indeed occupying the iron 3d type orbitals. More specifically, one electron occupies a nearly pure  $d_{x^2}$  orbital in the  $13\text{a}_1$  orbital. A second unpaired electron can be found in the  $5\text{b}_1$  orbital with predominant  $d_{xz}$  character, while  $2\text{a}_2$  as a similar  $d_{xy}$  orbital hosts the third unpaired electron. For  $\text{D}_{3\text{h}}$  geometries,  $d_{x^2}$  is totally symmetric ( $\text{a}_1'$ ), whereas the latter two d orbitals form a basis for the  $e''$  irreducible representation. The remaining two d orbitals are depicted as  $14\text{a}_1$  ( $d_{y^2-z^2}$ ) and  $8\text{b}_2$  ( $d_{yz}$ ). They are not occupied in any of the states relevant to the photoelectron spectrum because they are positioned at much higher energies. These d orbitals belong to an antibonding 2-fold degenerate  $e'$  level. Molecular orbitals with predominant oxygen contributions are without any exception doubly occupied. Pure  $\sigma$  binding interaction between iron and oxygen is present in the  $10\text{a}_1$ ,  $12\text{a}_1$ , and  $5\text{b}_2$  orbitals. The other predominant oxygen orbitals are either pure  $\pi$  bonding orbitals, i.e.,  $3\text{b}_1$ ,  $4\text{b}_1$ ,  $7\text{b}_2$ , and  $1\text{a}_2$ , or a mixture of the two types of bonding:  $11\text{a}_1$  and  $6\text{b}_2$ . All of these orbitals are to an extremely large extent constructed from the 2p orbitals of the oxygen atoms. Since the 2s orbitals of these atoms are all in the inactive space, the electronic structure picture emerging from the above orbitals puts a formal charge of +5 on iron and –2 on each oxygen center. All of the other low-lying states of the anionic cluster were found to agree with this picture. A similar orbital analysis for the relevant  $\text{FeO}_3$  states agrees completely with the above orbital picture for  $\text{FeO}_3^-$ , which therefore renders a formal oxidation state of +6 for the metal atom in the neutral cluster. For the neutral iron trioxide cluster, the same conclusion regarding the oxidation state of iron was put forward by Gong and Zhou after analyzing their DFT

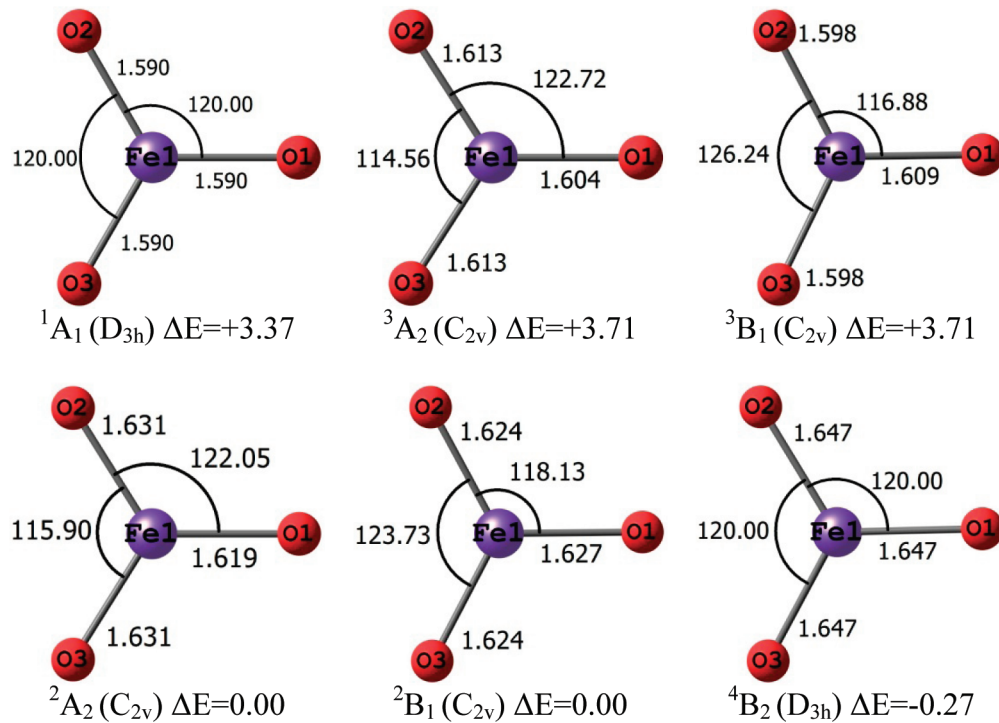


**Figure 3.** Structures (bond distances in Ångstroms and bond angles in degrees) and relative energies (eV) for the low lying states of FeO<sub>3</sub> and FeO<sub>3</sub><sup>-</sup> as obtained by CASPT2 geometry optimizations.

**Table 2.** Relative CASPT2 Energies for the Iron Trioxides FeO<sub>3</sub> and FeO<sub>3</sub><sup>-</sup>

cluster	state	relative energy (eV)		
		a	b	c
FeO <sub>3</sub> <sup>-</sup>	<sup>2</sup> A <sub>2</sub>	0.00	0.00	0.00
	<sup>2</sup> B <sub>1</sub>		0.00	0.02
	<sup>4</sup> B <sub>2</sub>	-0.26	-0.27	-0.25
	<sup>1</sup> A <sub>1</sub>	3.40	3.37	3.44
	<sup>3</sup> A <sub>2</sub>	3.74	3.71	3.77
	<sup>3</sup> B <sub>1</sub>		3.71	3.77
FeO <sub>3</sub>	<sup>2</sup> A <sub>2</sub>	0.00	0.00	0.00
	<sup>2</sup> B <sub>1</sub>		0.00	0.02
	<sup>4</sup> B <sub>2</sub>	-0.26	-0.27	-0.25
	<sup>1</sup> A <sub>1</sub>	3.40	3.37	3.44
	<sup>3</sup> A <sub>2</sub>	3.74	3.71	3.77
	<sup>3</sup> B <sub>1</sub>		3.71	3.77

<sup>a</sup> ASPT2 single point calculations with small ANO-RCC basis sets at BP/QZVP geometries. <sup>b</sup> CASPT2 geometry optimizations with small ANO-RCC basis sets. <sup>c</sup> CASPT2 single point calculation with large ANO-RCC basis sets at geometries b.

**Table 3.** Mulliken Population Analysis Charges for Low-Lying States of the FeO<sub>3</sub> and FeO<sub>3</sub><sup>-</sup> Clusters As Obtained from the CASPT2 Wave Functions

state	Mulliken charge (e <sup>-</sup> )			
	Fe	O(1)	O(2)	O(3)
<sup>2</sup> A <sub>2</sub>	+0.91	-0.59	-0.66	-0.66
<sup>2</sup> B <sub>1</sub>	+0.97	-0.70	-0.63	-0.63
<sup>4</sup> B <sub>2</sub>	+1.13	-0.71	-0.71	-0.71
<sup>1</sup> A <sub>1</sub>	+1.10	-0.37	-0.37	-0.37
<sup>3</sup> A <sub>2</sub>	+1.24	-0.40	-0.42	-0.42
<sup>3</sup> B <sub>1</sub>	+1.29	-0.45	-0.42	-0.42

results.<sup>15</sup> Formally, the ionization processes that lie beneath the photoelectron spectrum of FeO<sub>3</sub><sup>-</sup> involve the removal of an iron 3d electron, a result that is apparently in sharp contrast to the previous DFT study.<sup>14</sup> Compared to FeO<sub>3</sub> and on the basis of a natural bond analysis of the DFT orbitals, the extra electron of FeO<sub>3</sub><sup>-</sup> was found by these authors to be delocalized over the oxygens. So, at first sight, a formal description of the electronic structure and an analysis of the

**Table 4.** Vertical Detachment Energies (VDE) from the <sup>4</sup>B<sub>2</sub> State As Calculated by CASPT2 with Small ANO-RCC Basis Sets

Cluster	State	Leading Configuration CASSCF <sup>a</sup>	VDE (eV)
FeO <sub>3</sub> <sup>-</sup>	<sup>4</sup> A <sub>1</sub>	11a <sub>1</sub> <sup>2</sup> 12a <sub>1</sub> <sup>2</sup> 13a <sub>1</sub> <sup>2</sup> 14a <sub>1</sub> <sup>0</sup> 4b <sub>1</sub> <sup>2</sup> 5b <sub>1</sub> <sup>1</sup> 6b <sub>2</sub> <sup>1</sup> 7b <sub>2</sub> <sup>2</sup> 8b <sub>2</sub> <sup>0</sup> 2a <sub>2</sub> <sup>1</sup>	1.74
	<sup>4</sup> A <sub>2</sub>	11a <sub>1</sub> <sup>2</sup> 12a <sub>1</sub> <sup>2</sup> 13a <sub>1</sub> <sup>1</sup> 14a <sub>1</sub> <sup>1</sup> 4b <sub>1</sub> <sup>2</sup> 5b <sub>1</sub> <sup>0</sup> 6b <sub>2</sub> <sup>2</sup> 7b <sub>2</sub> <sup>2</sup> 8b <sub>2</sub> <sup>0</sup> 2a <sub>2</sub> <sup>1</sup>	3.14
	<sup>4</sup> B <sub>1</sub>	11a <sub>1</sub> <sup>2</sup> 12a <sub>1</sub> <sup>2</sup> 13a <sub>1</sub> <sup>1</sup> 14a <sub>1</sub> <sup>0</sup> 4b <sub>1</sub> <sup>2</sup> 5b <sub>1</sub> <sup>0</sup> 6b <sub>2</sub> <sup>2</sup> 7b <sub>2</sub> <sup>2</sup> 8b <sub>2</sub> <sup>1</sup> 2a <sub>2</sub> <sup>1</sup>	1.69
	<sup>4</sup> B <sub>2</sub>	11a <sub>1</sub> <sup>2</sup> 12a <sub>1</sub> <sup>2</sup> 13a <sub>1</sub> <sup>1</sup> 14a <sub>1</sub> <sup>0</sup> 4b <sub>1</sub> <sup>2</sup> 5b <sub>1</sub> <sup>1</sup> 6b <sub>2</sub> <sup>2</sup> 7b <sub>2</sub> <sup>2</sup> 8b <sub>2</sub> <sup>0</sup> 2a <sub>2</sub> <sup>1</sup>	0.00
	<sup>3</sup> A <sub>1</sub>	11a <sub>1</sub> <sup>2</sup> 12a <sub>1</sub> <sup>2</sup> 13a <sub>1</sub> <sup>1</sup> 14a <sub>1</sub> <sup>0</sup> 4b <sub>1</sub> <sup>2</sup> 5b <sub>1</sub> <sup>1</sup> 6b <sub>2</sub> <sup>1</sup> 7b <sub>2</sub> <sup>2</sup> 8b <sub>2</sub> <sup>0</sup> 2a <sub>2</sub> <sup>1</sup>	4.93
	<sup>3</sup> A <sub>2</sub>	11a <sub>1</sub> <sup>2</sup> 12a <sub>1</sub> <sup>2</sup> 13a <sub>1</sub> <sup>1</sup> 14a <sub>1</sub> <sup>0</sup> 4b <sub>1</sub> <sup>2</sup> 5b <sub>1</sub> <sup>0</sup> 6b <sub>2</sub> <sup>2</sup> 7b <sub>2</sub> <sup>2</sup> 8b <sub>2</sub> <sup>0</sup> 2a <sub>2</sub> <sup>1</sup>	4.06
FeO <sub>3</sub>	<sup>3</sup> B <sub>1</sub>	11a <sub>1</sub> <sup>2</sup> 12a <sub>1</sub> <sup>2</sup> 13a <sub>1</sub> <sup>1</sup> 14a <sub>1</sub> <sup>0</sup> 4b <sub>1</sub> <sup>2</sup> 5b <sub>1</sub> <sup>1</sup> 6b <sub>2</sub> <sup>2</sup> 7b <sub>2</sub> <sup>2</sup> 8b <sub>2</sub> <sup>0</sup> 2a <sub>2</sub> <sup>0</sup>	4.06
	<sup>3</sup> B <sub>2</sub>	11a <sub>1</sub> <sup>2</sup> 12a <sub>1</sub> <sup>2</sup> 13a <sub>1</sub> <sup>1</sup> 14a <sub>1</sub> <sup>0</sup> 4b <sub>1</sub> <sup>2</sup> 5b <sub>1</sub> <sup>0</sup> 6b <sub>2</sub> <sup>2</sup> 7b <sub>2</sub> <sup>2</sup> 8b <sub>2</sub> <sup>1</sup> 2a <sub>2</sub> <sup>0</sup>	5.64
	<sup>5</sup> A <sub>1</sub>	11a <sub>1</sub> <sup>2</sup> 12a <sub>1</sub> <sup>2</sup> 13a <sub>1</sub> <sup>1</sup> 14a <sub>1</sub> <sup>0</sup> 4b <sub>1</sub> <sup>2</sup> 5b <sub>1</sub> <sup>1</sup> 6b <sub>2</sub> <sup>1</sup> 7b <sub>2</sub> <sup>2</sup> 8b <sub>2</sub> <sup>0</sup> 2a <sub>2</sub> <sup>1</sup>	4.82
	<sup>5</sup> A <sub>2</sub>	11a <sub>1</sub> <sup>2</sup> 12a <sub>1</sub> <sup>2</sup> 13a <sub>1</sub> <sup>1</sup> 14a <sub>1</sub> <sup>0</sup> 4b <sub>1</sub> <sup>1</sup> 5b <sub>1</sub> <sup>1</sup> 6b <sub>2</sub> <sup>2</sup> 7b <sub>2</sub> <sup>2</sup> 8b <sub>2</sub> <sup>1</sup> 2a <sub>2</sub> <sup>1</sup>	5.47
	<sup>5</sup> B <sub>1</sub>	11a <sub>1</sub> <sup>2</sup> 12a <sub>1</sub> <sup>2</sup> 13a <sub>1</sub> <sup>1</sup> 14a <sub>1</sub> <sup>1</sup> 4b <sub>1</sub> <sup>2</sup> 5b <sub>1</sub> <sup>0</sup> 6b <sub>2</sub> <sup>1</sup> 7b <sub>2</sub> <sup>2</sup> 8b <sub>2</sub> <sup>0</sup> 2a <sub>2</sub> <sup>1</sup>	6.29
	<sup>5</sup> B <sub>2</sub>	11a <sub>1</sub> <sup>2</sup> 12a <sub>1</sub> <sup>2</sup> 13a <sub>1</sub> <sup>1</sup> 14a <sub>1</sub> <sup>0</sup> 4b <sub>1</sub> <sup>2</sup> 5b <sub>1</sub> <sup>1</sup> 6b <sub>2</sub> <sup>2</sup> 7b <sub>2</sub> <sup>2</sup> 8b <sub>2</sub> <sup>0</sup> 2a <sub>2</sub> <sup>1</sup>	5.89
<sup>1</sup> B <sub>2</sub>	<sup>1</sup> B <sub>2</sub>	11a <sub>1</sub> <sup>2</sup> 12a <sub>1</sub> <sup>2</sup> 13a <sub>1</sub> <sup>0</sup> 14a <sub>1</sub> <sup>0</sup> 4b <sub>1</sub> <sup>2</sup> 5b <sub>1</sub> <sup>1</sup> 6b <sub>2</sub> <sup>2</sup> 7b <sub>2</sub> <sup>2</sup> 8b <sub>2</sub> <sup>0</sup> 2a <sub>2</sub> <sup>1</sup>	5.57
	<sup>2</sup> B <sub>2</sub>	11a <sub>1</sub> <sup>2</sup> 12a <sub>1</sub> <sup>2</sup> 13a <sub>1</sub> <sup>0</sup> 14a <sub>1</sub> <sup>0</sup> 4b <sub>1</sub> <sup>2</sup> 5b <sub>1</sub> <sup>0</sup> 6b <sub>2</sub> <sup>2</sup> 7b <sub>2</sub> <sup>2</sup> 8b <sub>2</sub> <sup>1</sup> 2a <sub>2</sub> <sup>0</sup>	5.82

<sup>a</sup> In the leading configuration, the 10a<sub>1</sub>, 3b<sub>1</sub>, 5b<sub>2</sub>, and 1a<sub>1</sub> orbitals are always doubly occupied; the 15a<sub>1</sub> orbital is always unoccupied.

distribution of the electrons over the constituent atoms lead to opposing underlying electron detachment processes. An explanation for this discrepancy is given by a Mulliken

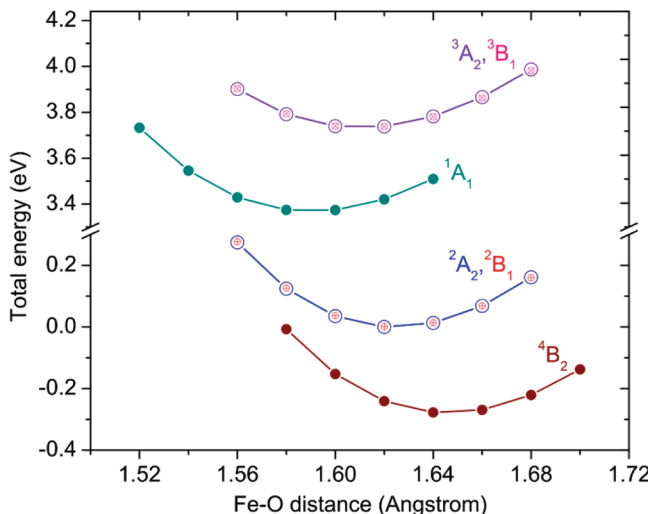


**Figure 4.** CASPT2 (using small ANO-RCC basis sets) potential energy curves of the symmetric Fe–O bond stretch ( $D_{3h}$  symmetry).

population analysis of the CASPT2 wave functions, which is given in Table 3. In agreement with the DFT description, the charge on the iron atom is hardly different between the anionic and neutral states. The formal removal of an electron for either three-occupied d orbital is compensated by small but effective relaxations in the underlying closed shell oxygen orbitals, which increase the  $\sigma$  and  $\pi$  ligand to metal donation of electronic charge. For a localization of charges within the molecules, a population analysis is therefore more trustworthy. The formal description of the electronic structure however has its merits in the sense that it provides a qualitative understanding of the relative position of the low-lying states of both species, as we will illustrate in the next paragraph.

The above description of the electronic structure closely resembles that of the classical and well-known transition metal complexes. For this type of compound, the electronic structure has, for decades, very successfully been described by qualitative ligand field theory. Within this model, the lower lying ligand ( $\text{O}^{2-}$  ions in present case) valence orbitals interact with the higher positioned d orbitals of the metal and become bonding molecular orbitals. For planar  $D_{3h}$  complexes, the ligand field model leads to the characteristic energy pattern in which the higher energy antibonding d orbitals are split into three levels (Figure 1). A lowest almost nonbonding orbital is only weakly  $\sigma$  antibonding, as illustrated for  $13\text{a}_1$  in Figure 5. In the middle, we find an exclusively  $\pi$  antibonding  $e''$  level ( $5\text{b}_1$  and  $2\text{a}_2$  orbitals in Figure 5). The highest d level corresponds to the  $14\text{a}_1$  and  $8\text{b}_2$  orbitals of the mainly  $\sigma$  antibonding  $e'$  shell. For  $\text{FeO}_3^-$ , the remaining three metal valence electrons are to be distributed among the lowest d orbitals. For the anion, the first candidate ground state is found by placing two electrons in the lowest  $13\text{a}_1$  orbital and the remaining electron in either one of the two  $d_\pi$  ( $5\text{b}_1$  or  $2\text{a}_2$ ) orbitals, giving rise to a so-called low-spin  $^2\text{E}''$  state, which is Jahn–Teller active. The occupation of the antibonding  $d_{xy}$  ( $2\text{a}_2$ ) orbital induces an increase in two O–Fe–O bond angles and an increase in two Fe–O bond distances, to which this orbital is oriented.

This is the result of the increased electrostatic interactions between the approaching oxygen atoms and the antibonding nature of the  $2\text{a}_2$  orbital. The entry for the  $^2\text{A}_2$  of Figure 3 is in accordance with this analysis. The occupation, on the other hand, of  $d_{xz}$  ( $5\text{b}_1$ ) causes one bond angle to increase, which stabilizes the  $^2\text{B}_1$  component. Opening up two bonds is apparently more favorable, which makes the  $^2\text{A}_2$  component the lowest in energy. The second candidate ground state is found by distributing the three valence metal electrons equally among the three lowest orbitals with the same spin. The resulting  $^4\text{B}_2$  ( $^4\text{A}_1$  in  $D_{3h}$ ) has a high-spin state with a lower electron repulsion and is predicted by CASPT2 as the ground state of  $\text{FeO}_3^-$ . For the neutral cluster, we expect two low lying states. The first one places two valence electrons in the lowest  $d_{x^2}$  orbital, giving a  $^1\text{A}_1$  state, which is always predicted as the ground state. The first excited state is a  $^3\text{E}''$  with an occupation of  $(d_{x^2})^1(d_{xy}, d_{yz})^1$ . Quintets are expected at much higher energies because they involve an ionization process from one of the low-lying oxygen 2p orbitals. Thus, we suppose that they have no relevance to the low-energy part of the photoelectron spectrum. In this context, the above ligand field picture for these complexes attributes important roles to the  $^1\text{A}_1$  and the  $^3\text{E}''$  states of the neutral complex.

The photoelectron spectrum of  $\text{FeO}_3^-$  measured with 4.66 eV laser photon energy, shown in Figure 6, has two low-lying bands.<sup>9–12</sup> The first band starts at 3.26 eV (X band), and the second band is located at higher binding energies (A band). The structure of the X band is composed of three sharp peaks of more or less equal intensity. Together, they are proposed to form a vibrational progression. The A band consists of two peaks, of which the first one at 3.81 eV has a much larger intensity than the higher energy peak. Both states of  $\text{FeO}_3$  are measured to have a vibrational frequency of  $850 \text{ cm}^{-1}$ . These two simple vibrational structures indicate, according to the authors, that the geometries of  $\text{FeO}_3$  and  $\text{FeO}_3^-$  possess a high level of symmetry like  $D_{3h}$ . Further, it was argued that the observed electron detachment processes induce only very slight geometry changes along the Fe–O stretching coordinate. On a qualitative basis, our DFT and CASPT2 geometry optimizations confirm these conclusions. Indeed, due to the extremely small Jahn–Teller effects, all of the states of the neutral and the anionic iron trioxide species that are relevant to the photoelectron either possess a  $D_{3h}$  structure (spacial nondegenerate states) or only slightly deviate from it (spacial degenerate states). In the latter case, the energy barriers that connect the two minima of a Jahn–Teller active state of  $D_{3h}$  symmetry are evaluated by CASPT2 as being very small. In regard to vibrational considerations, these states can be seen as having the higher  $D_{3h}$  symmetry, and therefore the assignment of the photoelectron spectrum should be carried out on these grounds. To answer the question of which state of  $\text{FeO}_3^-$  is responsible for its photoelectron spectrum, we calculated the one electron ADEs and VDEs from the  $^2\text{E}''$  and  $^4\text{A}_1$  states.

According to the CASPT2 results,  $^4\text{A}_1$  has the lowest energy of  $\text{FeO}_3^-$ , so we need to explore the ionizations from this state first. Following the one-electron detachment selection rule, we only need to consider triplet and quintet

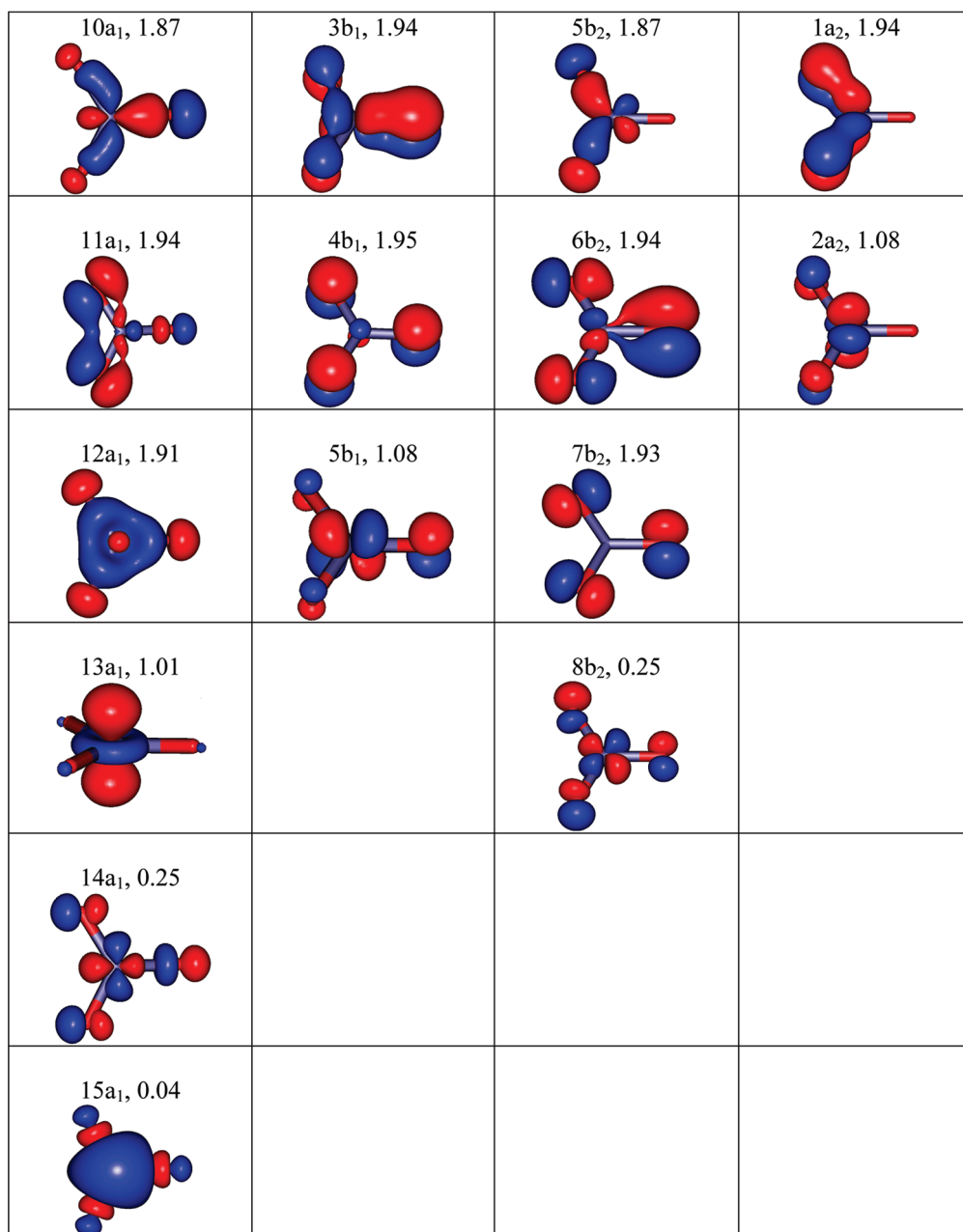


**Figure 5.** Pseudonatural molecular orbital plots and their occupation numbers for the  $^4B_2$  state ( $\text{FeO}_3^-$ ) as calculated by CASSCF (small ANO-RCC basis sets).

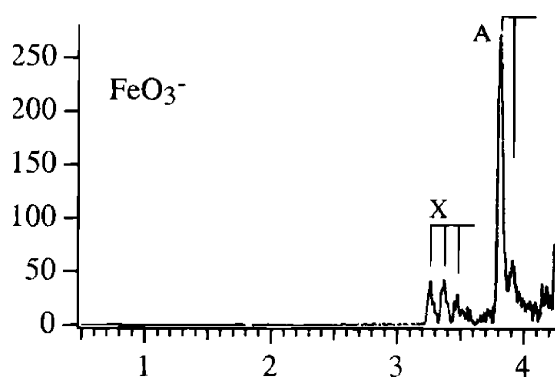


**Figure 6.** Photoelectron spectrum of  $\text{FeO}_3^-$  taken from ref 10. Abscissa: binding energies in electronvolts. Ordinate: relative electron intensities.

states. Table 4 summarizes the lowest VDEs for each irreducible representation of  $C_{2v}$  and relevant spin multiplicities. As a first conclusion, we note that the VDEs needed to reach the quintets are much higher than those for the triplets, a finding that already could be made from our DFT calculations and in agreement with the previous computational study.<sup>14</sup> Our results point out that removing one electron from the configuration of  $^4A_1'$  (or  $^4B_2$  in  $C_{2v}$ ) can give only the following low-lying  $C_{2v}$  triplet states:  $^3A_2$  and  $^3B_1$ . The removal of an electron from the  $5b_1$  orbital of  $^4B_2$  creates  $^3A_2$ , whereas an ionization from the  $2a_2$  orbital results in the  $^3B_1$  state of the neutral system. As a consequence of the small energetic Jahn–Teller effects, both transitions occur with a VDE value of 4.06 eV, and they could correspond to the A band in photoelectron spectrum of  $\text{FeO}_3^-$ . The quintet states  $^5A_1$ ,  $^5A_2$ , and  $^5B_2$  can also be formed by a one-electron

**Table 5.** Vertical Detachment Energies (VDE) from the  $^2\text{A}_2$  State As Calculated by (a) CASPT2 with Small ANO-RCC Basis Sets and (b) CASPT2 with Large ANO-RCC Basis Sets<sup>a</sup>

cluster	state	leading configuration CASSCF	VDE (eV)		exp (eV)
			a	b	
$\text{FeO}_3^-$	$^2\text{A}_1$	$11\text{a}_1^2 12\text{a}_1^2 13\text{a}_1^1 14\text{a}_1^0 4\text{b}_1^2 5\text{b}_1^0$	1.03		
		$6\text{b}_2^2 7\text{b}_2^2 8\text{b}_2^0 2\text{a}_2^2$			
	$^2\text{A}_2$	$11\text{a}_1^2 12\text{a}_1^2 13\text{a}_1^2 14\text{a}_1^0 4\text{b}_1^2 5\text{b}_1^0$	0.00		
		$6\text{b}_2^2 7\text{b}_2^2 8\text{b}_2^0 2\text{a}_2^1$			
$\text{FeO}_3^-$	$^2\text{B}_1$	$11\text{a}_1^2 12\text{a}_1^2 13\text{a}_1^2 14\text{a}_1^0 4\text{b}_1^2 5\text{b}_1^1$	0.12		
		$6\text{b}_2^2 7\text{b}_2^2 8\text{b}_2^0 2\text{a}_2^0$			
	$^2\text{B}_2$	$11\text{a}_1^2 12\text{a}_1^2 13\text{a}_1^1 14\text{a}_1^0 4\text{b}_1^2 5\text{b}_1^1$	0.75		
		$6\text{b}_2^2 7\text{b}_2^2 8\text{b}_2^0 2\text{a}_2^1$			
$\text{FeO}_3^-$	$^1\text{A}_1$	$11\text{a}_1^2 12\text{a}_1^2 13\text{a}_1^2 14\text{a}_1^0 4\text{b}_1^2 5\text{b}_1^0$	3.46	3.54	3.26
		$6\text{b}_2^2 7\text{b}_2^2 8\text{b}_2^0 2\text{a}_2^0$			
	$^1\text{A}_2$	$11\text{a}_1^2 12\text{a}_1^2 13\text{a}_1^1 14\text{a}_1^0 4\text{b}_1^2 5\text{b}_1^1$	5.17		
		$6\text{b}_2^2 7\text{b}_2^2 8\text{b}_2^0 2\text{a}_2^0$			
	$^1\text{B}_1$	$11\text{a}_1^2 12\text{a}_1^2 13\text{a}_1^2 14\text{a}_1^0 4\text{b}_1^2 5\text{b}_1^0$	5.05		
		$6\text{b}_2^2 7\text{b}_2^2 8\text{b}_2^0 2\text{a}_2^1$			
	$^1\text{B}_2$	$11\text{a}_1^2 12\text{a}_1^2 13\text{a}_1^1 14\text{a}_1^0 4\text{b}_1^2 5\text{b}_1^0$	5.69		
		$6\text{b}_2^2 7\text{b}_2^2 8\text{b}_2^0 2\text{a}_2^2$			
	$^3\text{A}_1$	$11\text{a}_1^2 12\text{a}_1^2 13\text{a}_1^1 14\text{a}_1^0 4\text{b}_1^2 5\text{b}_1^1$	4.73		
		$6\text{b}_2^2 7\text{b}_2^2 8\text{b}_2^0 2\text{a}_2^1$			
	$^3\text{A}_2$	$11\text{a}_1^2 12\text{a}_1^2 13\text{a}_1^1 14\text{a}_1^0 4\text{b}_1^2 5\text{b}_1^0$	3.73	3.80	3.81
		$6\text{b}_2^2 7\text{b}_2^2 8\text{b}_2^0 2\text{a}_2^1$			
$\text{FeO}_3^-$	$^3\text{B}_1$	$11\text{a}_1^2 12\text{a}_1^2 13\text{a}_1^1 14\text{a}_1^0 4\text{b}_1^2 5\text{b}_1^1$	3.85		3.81
		$6\text{b}_2^2 7\text{b}_2^2 8\text{b}_2^0 2\text{a}_2^0$			
	$^3\text{B}_2$	$11\text{a}_1^2 12\text{a}_1^2 13\text{a}_1^0 14\text{a}_1^0 4\text{b}_1^2 5\text{b}_1^0$	5.57		
		$6\text{b}_2^2 7\text{b}_2^2 8\text{b}_2^1 2\text{a}_2^0$			
$\text{FeO}_3^-$	$^1\text{B}_{2g}$	$11\text{a}_1^2 12\text{a}_1^2 13\text{a}_1^0 14\text{a}_1^0 4\text{b}_1^2 5\text{b}_1^1$	5.30		
		$6\text{b}_2^2 7\text{b}_2^2 8\text{b}_2^0 2\text{a}_2^1$			
$\text{FeO}_3^-$	$^2\text{B}_{2g}$	$11\text{a}_1^2 12\text{a}_1^2 13\text{a}_1^1 14\text{a}_1^0 4\text{b}_1^2 5\text{b}_1^0$	5.75		
		$6\text{b}_2^2 7\text{b}_2^2 8\text{b}_2^1 2\text{a}_2^0$			

<sup>a</sup> In the leading configuration, the  $10\text{a}_1$ ,  $3\text{b}_1$ ,  $5\text{b}_2$ , and  $1\text{a}_1$  orbitals are always doubly occupied; the  $15\text{a}_1$  orbital is always unoccupied.

detachment out of the  $6\text{b}_2$ ,  $4\text{b}_1$ , and  $12\text{a}_1$  orbitals of  $^4\text{B}_2$ , respectively. However, the corresponding VDEs for these ionizations are 4.82, 5.47, and 5.89 eV, and therefore they are much too high to explain the low-energy part of the photoelectron spectrum. Clearly, the X band cannot be explained by a one-electron ionization process from the  $^4\text{B}_2$  state of  $\text{FeO}_3^-$ , and we need to explore other states of the anion.

Obviously, the next states of  $\text{FeO}_3^-$  that can be at the origin of its photoelectron spectroscopy are the nearly degenerate  $^2\text{A}_2$  and  $^2\text{B}_1$  components of the  $D_{3h}^2\text{E}''$  state. Both the  $C_{2v}$  states have a slightly different equilibrium geometry, which explains the 0.12 eV vertical energy difference for  $^2\text{B}_1$  in Table 5, which contains the CASPT2 energies from single point calculations on the geometry of the lower  $^2\text{A}_2$  component. This contrasts with Table 4, which was obtained from the single point  $D_{3h}$  calculation using the Jahn–Teller inactive  $^4\text{B}_2$  geometry. Starting from the  $^2\text{A}_2$  and  $^2\text{B}_1$  states, we can obtain the ground state  $^1\text{A}_1$  of  $\text{FeO}_3$  through a one-electron removal from the  $2\text{a}_2$  and  $5\text{b}_1$  orbitals, respectively. As advocated in a previous paragraph, the small energy barrier connecting the  $^2\text{A}_2$  and  $^2\text{B}_1$  states and the resulting vibronic coupling will give rise to a single band in the experimental spectrum, which we could describe as the  $D_{3h}$  transition  $^2\text{E}'' \rightarrow ^1\text{A}_1$ . Solely for computational convenience, we only included VDEs from the  $^2\text{A}_2$  lowest energy component, which has

certainly no bearing whatsoever on the proposed conclusions. The corresponding ADE and VDE values for this process are 3.37 and 3.46 eV, and we believe this transition is at the origin of the X band at 3.26 eV of the experimental spectrum. Moreover, if we remove one electron from the  $13\text{a}_1$  orbital of  $^2\text{A}_2$ , we arrive at the  $^3\text{A}_2$  state, for which the ADE and VDE values are 3.71 and 3.73 eV. These energies correspond very well with the A band at 3.81 eV. Judging from Table 5, we strongly believe that we could have drawn exactly the same conclusion from VDEs obtained for ionizations from the  $^2\text{B}_1$  component. On the basis of all of the above arguments, we are inclined to make the following proposition about the photoelectron spectrum of  $\text{FeO}_3^-$ . The two low-lying bands should be assigned as originating from the  $^2\text{E}''$  ( $^2\text{A}_2$  and  $^2\text{B}_1$ ) state of  $\text{FeO}_3^-$ , although our CASPT2 places this state at a higher energy of about 0.27 eV than  $^4\text{A}_1'$ . In order to get better values for the ADEs and VDEs, we performed single point CASPT2 calculations with larger ANO-RCC [8s,7p,6d,4f,2g,1h] and [7s,6p,4d,3f,1g] basis sets for iron and oxygen, respectively. At this computational level, the VDE for the X feature is 3.54 eV, while for the A feature, we find 3.80 eV.  $^4\text{A}_1'$  remains the ground state at this level, and the energy gap of 0.25 eV with  $^2\text{A}_2$  ( $^2\text{E}''$ ) is hardly affected.

Further evidence for the above proposed assignment can be obtained from the observed peak intensities in the vibrational progressions. As mentioned, the X feature is a broad progression of four peaks of relatively low intensity, which implies that there is a relatively larger difference between the geometries of the anionic  $\text{FeO}_3^-$  state and the final  $\text{FeO}_3$  state. Otherwise, the A feature has a high-intensity sharp peak and a much lower second one, indicative of a smaller geometric difference between the geometries of two states that are responsible for this band. Also, the distinct vibrational progressions in the experimental spectrum strongly suggest that just one vibration mode lies at their origin. The rather large values of the associated vibrational frequencies of  $850\text{ cm}^{-1}$  suggest a Fe–O stretching mode as observed for the diatomic  $\text{FeO}$ .<sup>9–12,14,15,25</sup> On this premise and using the potential energy curves of Figure 4, we can perform a harmonic vibration analysis for the symmetric stretching mode of the various low-lying states incorporated in this figure. The calculated Franck–Condon factors are depicted in Figure 7. For the lowest electron detachment, a vibrational frequency of  $927\text{ cm}^{-1}$  was obtained for the  $^1\text{A}_1'$  ground state of the neutral system, which corresponds well with the DFT value of  $920\text{ cm}^{-1}$  from Table 1. Compared to the experimental  $850\text{ cm}^{-1}$  from the photoelectron spectrum, it lies just outside the proposed error margin of  $50\text{ cm}^{-1}$ . Further on, Figure 7a shows three Franck–Condon factors of more than 0.1, which agrees with the observed vibrational progression of the X band. Taking into account that our result is just a first estimate for the frequency, we interpret these results as a confirmation of the proposed assignment for this band. An even better correspondence was found for the A band. The calculated frequency of  $881\text{ cm}^{-1}$  for the  $^3\text{A}_2$  state is in

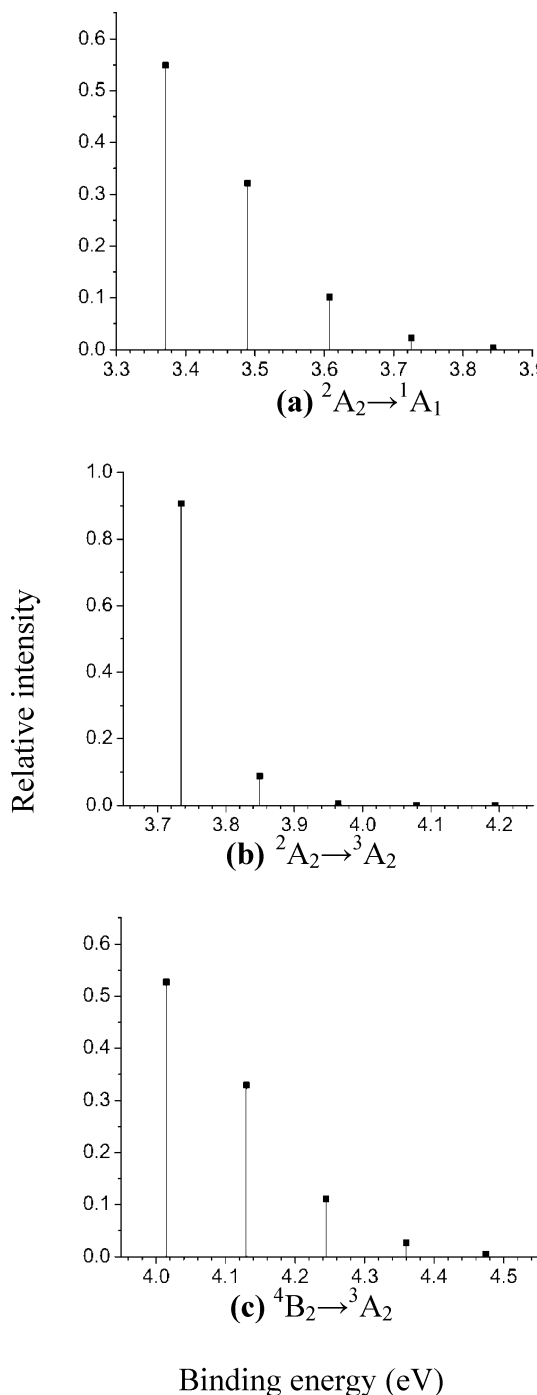


**Figure 7.** Simulated vibrational progression on the basis of harmonic Franck–Condon factors for the symmetric stretch of the three lowest energy electron detachment processes. Peak positions derived from CASPT2 energies, BP/QZVP zero-point energies, and CASPT2 symmetric stretch frequencies.

complete agreement with the experimental value of 850 (50)  $\text{cm}^{-1}$  but somewhat at variance with the DFT result of 995  $\text{cm}^{-1}$ . According to Figure 7b, the Franck–Condon factors for this band indicate just two observable peaks, in which the low energy one is about 10 times more intensive, a good match with the experimental spectrum of Figure 6. By studying the shapes of low-lying bands as above, we conclude that only the  $^2\text{E}''$  lies at the origin of the photoelectron spectrum of  $\text{FeO}_3^-$ , and that detach-

ments to the  $^1\text{A}'$  and  $^3\text{E}''$  states of the neutral complex are responsible for the X and A bands, respectively.

## Conclusion

For the first time, the electronic structures of  $\text{FeO}_3$  stoichiometry have been investigated at a multireference level of theory. We have found several stable geometries for both the singly charged anionic and neutral structures with different spin multiplicities. Regardless of the charge of these complexes, the  $\eta^2\text{-O}_2\text{FeO}$  conformations with O–O bonding are much higher in energy than the corresponding lowest iron trioxide conformations without any direct O–O bonding. Due to small Jahn–Teller effects, all of the equilibrium geometries of the latter conformation and the resulting photoelectron spectrum can effectively be described by using the planar  $\text{D}_{3\text{h}}$  symmetry. The computed CASSCF molecular orbitals as well as a qualitative interpretation of the relative CASPT2 energies unambiguously point to a formal oxidation state of +6 and +5 of iron in the neutral and anionic species, respectively. These oxidation states for both species imply that the ionization processes that underlie the bands observed in the experimental photoelectron spectrum correspond formally to a detachment of a metal electron. However, a population analysis of the ab initio wave functions shows that, most likely, the observed ionization processes involve the removal of electron density from the oxygen atoms. Quite remarkable, a general analysis in terms of a simply ligand field description of the splitting pattern of the valence iron 3d orbitals is effective to describe the electronic structure of the clusters and their studied spectroscopy. The ground state of the neutral cluster is the closed shell  $^1\text{A}'$ , but the lowest state of the anion can be either the strong-field ground state or low-spin  $^2\text{E}''$  ( $^2\text{A}_2$ ,  $^2\text{B}_1$ ) or the weak-field ground state or high-spin  $^4\text{A}'$ . A 0.25 eV energy gap between them is judged to be too small to conclude unequivocally which is the true ground state of the anion, although the latter state should be seen as a serious candidate. From our CASPT2 calculations, we are inclined to assign the low-lying bands of the photoelectron spectrum of  $\text{FeO}_3^-$  as electron detachment processes from the low-spin  $^2\text{E}''$  state. Our best VDEs (ADEs) values are 3.54 (3.44) eV and 3.80 (3.77) eV, which compare convincingly well with the start position of the X band at 3.26 eV and of the A band at 3.81 eV. The closed shell ground state  $^1\text{A}'$  and the first excited state  $^3\text{E}''$  of the neutral cluster lie at the origin of these two bands. Analyzing the vibrational progression of these transitions further substantiates our proposed assignment.

**Acknowledgment.** This study has been supported by grants from the Flemish Science Foundation (FWO) and from the Concerted Research Action of the Flemish Government (GOA).

## References

- (1) Gong, Y.; Zhou, M.; Andrews, L. *Chem. Rev.* **2009**, *109*, 6765.
- (2) Jena, P.; Castleman, A. W., Jr. *Proc. Natl. Sci. U.S.A.* **2006**, *103*, 10560.
- (3) Mebel, A. M.; Hwang, D. Y. *J. Phys. Chem. A* **2001**, *105*, 7460.

- (4) Xue, W.; Wang, Z. C.; He, S.-G.; Xie, Y.; Bernstein, E. R. *J. Am. Chem. Soc.* **2008**, *30*, 15879.
- (5) El-Sheikh, S. M.; Harraz, F. A.; Abdel-Halim, K. S. *J. Alloy Compd.* **2009**, *487*, 716.
- (6) Fellah, M. F.; Onal, I.; van Santen, R. A. *J. Phys. Chem. C* **2010**, *114*, 12580.
- (7) Gutsev, G. L.; Bauschlicher, C. W., Jr. *Chem. Phys. Lett.* **2003**, *380*, 435.
- (8) Reddy, B. V.; Khanna, S. N. *Phys. Rev. Lett.* **2004**, *93*, 68301.
- (9) Fan, J.; Wang, L.-S. *J. Chem. Phys.* **1995**, *102*, 8714.
- (10) Wu, H.; Desai, S. R.; Wang, L.-S. *J. Am. Chem. Soc.* **1996**, *118*, 5296.
- (11) Wu, H.; Desai, S. R.; Wang, L.-S. *J. Am. Chem. Soc.* **1996**, *118*, 7434.
- (12) Wang, L.-S.; Wu, H.; Desai, S. R. *Phys. Rev. Lett.* **1996**, *76*, 4853.
- (13) Chertihin, G. V.; Saffel, W.; Yustein, J. T.; Andrews, L.; Neurock, M.; Ricca, A.; Bauschlicher, C. W., Jr. *J. Phys. Chem.* **1996**, *100*, 5261.
- (14) Gutsev, G. L.; Khanna, S. N.; Rao, B. K.; Jena, P. *J. Phys. Chem. A* **1999**, *103*, 5812.
- (15) Gong, Y.; Zhou, M. *J. Phys. Chem. A* **2008**, *112*, 10838.
- (16) Uzunova, E. L.; Milosch, H.; Nikolov, G. S. *J. Chem. Phys.* **2008**, *128*, 94307.
- (17) Clima, S.; Hendrickx, M. F. A. *Chem. Phys. Lett.* **2007**, *436*, 341.
- (18) Hübner, O.; Volker, T.; Berning, A.; Sauer, J. *Chem. Phys. Lett.* **1998**, *294*, 37.
- (19) Clima, S.; Hendrickx, M. F. A. *J. Phys. Chem. A* **2007**, *111*, 10992.
- (20) Gutsev, G. L.; Rao, B. K.; Jena, P. *J. Phys. Chem. A* **2000**, *104*, 5374.
- (21) Grein, F. I. *Int. J. Quantum Chem.* **2009**, *109*, 549.
- (22) Garcia-Sosa, A. T.; Castro, M. *Int. J. Quantum Chem.* **2000**, *80*, 307.
- (23) Schröder, D.; Kretzschaar, I.; Schwarz, H.; Rue, C.; Armen-trout, P. B. *Inorg. Chem.* **1999**, *38*, 3474.
- (24) Hübner, O.; Sauer, J. *J. Chem. Phys.* **2002**, *116*, 617.
- (25) Hendrickx, M. F. A.; Anam, K. R. *J. Phys. Chem. A* **2009**, *113*, 8746.
- (26) Cardoen, W.; Gdanitz, R. *J. Chem. Phys. Lett.* **2002**, *364*, 39.
- (27) Li, Z. H.; Gong, Y.; Fan, K.; Zhou, M. *J. Phys. Chem. A* **2008**, *112*, 13641.
- (28) Weigend, F.; Furche, F.; Ahlrichs, R. *J. Chem. Phys.* **2003**, *119*, 12753.
- (29) Ahlrichs, R.; Furche, F.; Grimme, S. *Chem. Phys. Lett.* **2000**, *325*, 317.
- (30) TURBOMOLE, V6.1 2009; University of Karlsruhe and Forschungszentrum Karlsruhe GmbH: Karlsruhe, Germany, 1989, TURBOMOLE GmbH since 2007. Available from <http://www.turbomole.com> (accessed Dec 9, 2010).
- (31) Karlström, G.; Lindh, R.; Malmqvist, P.-Å.; Roos, B. O.; Ryde, U.; Veryazov, V.; Widmark, P.-O.; Cossi, M.; Schimmelpfenning, B.; Neogrady, P.; Seijo, L. *Comput. Mater. Sci.* **2003**, *28*, 222.
- (32) Roos, B. O.; Lindh, R.; Malmqvist, P.-Å.; Veryazov, V.; Widmark, P.-O. *J. Phys. Chem. A* **2005**, *108*, 2851.
- (33) Douglas, N.; Kroll, N. M. *Ann. Phys.* **1974**, *82*, 89.
- (34) Hess, B. A. *Phys. Rev. A* **1986**, *33*, 3742.
- (35) Gutsev, G. L.; Khanna, S. N.; Rao, B. K.; Jena, P. *Phys. Rev. A* **1999**, *59*, 3681.
- (36) Gutsev, G. L.; Weatherford, C. A.; Pradhan, K.; Jena, P. *J. Phys. Chem. A* **2010**, *114*, 9014.

CT1005246